ADVANCED ENERGY MATERIALS

Supporting Information

for *Adv. Energy Mater.,* DOI: 10.1002/aenm.202103785

High-Frequency Light Rectification by Nanoscale Plasmonic Conical Antenna in Point-Contact-Insulator-Metal Architecture

Rajeshkumar Mupparapu, Joao Cunha, Francesco Tantussi, Andrea Jacassi, Leopold Summerer, Maddalena Patrini, Andrea Giugni, Lorenzo Maserati, Alessandro Alabastri, Denis Garoli, and Remo Proietti Zaccaria**

Supporting Information

High Frequency Light Rectification by Nanoscale Plasmonic Conical Antenna in Point-Contact-Insulator-Metal Architecture

Rajeshkumar Mupparapu, Joao Cunha, Francesco Tantussi, Andrea Jacassi, Leopold Summerer, Maddalena Patrini, Andrea Giugni, Alessandro Alabastri, Lorenzo Maserati, Denis Garoli, and Remo Proietti Zaccaria

Schematic of the set-up and experimental parameters

The schematic diagram of the overall setup is depicted in the **Figure S1** together with the MIM junction and the trans-impedance amplifier.

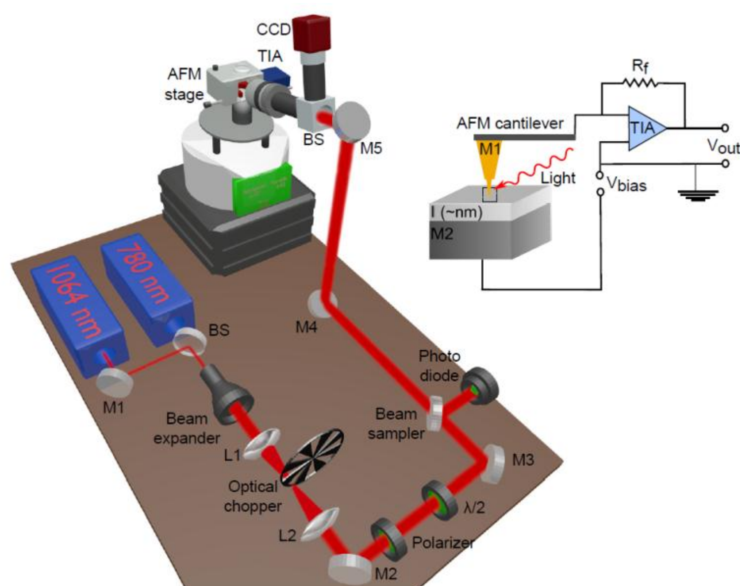

Figure S1. (left) 3D Schematic of the overall customized experimental configuration. (right) Schematic of the MIM junction positioned inside the AFM stage highlighting the trans-impedance amplifier (TIA) for filtering and data acquisition (i.e., analogic filter was employed for filtering, Ni-DAQ for data acquisition).

The experimental parameters regarding the laser illumination are summarized in **Table S1**:

Illumination parameter	Value	Value
Wavelength	1064 nm	780 nm

Polarization	90°	90°
Focal spot diameter	4 μm	5.25 μm
Angle of incidence	12° (w.r.t sample plane)	12° (w.r.t sample plane)
Input intensity	12.95 MW/m^2	7.1 MW/m^2

Table S1. Illumination conditions on the AFM tip.

The analogic filter settings are instead shown in **Table S2**:

Parameter	Value
Filter type	Bessel
Band	Low-pass
Cut-off frequency	10 kHz
Coupling	DC
Roll-off	12 dB/oct

Table S2. Settings of the analogic filter.

Optoelectronic measurements

The I-V characteristics of various nanorectanna samples were studied by applying a continuous slow sinusoidal bias voltage signal of certain amplitude to the bottom electrode of the pc-M1IM2 junction, while the current was recorded by the TIA, as previously described. Two different types of measurements, named Type 1 and Type 2, were performed on the pc-M1IM2 rectennas to obtain the I-V characteristic and the current generated exclusively due to the light illumination, respectively.

Type 1 measurement: This approach is characterized by fast acquisition of the I-V characteristic, in a time of just few seconds. The main motivation is related to the typical drift exhibited by AFM, which is due to thermal effects on the piezo. The drift exhibited by our Veeco AFM was of 9 nm/minute in X dimension and 5 nm/minute in Y dimension. In order to have stable measurements in time, a bias frequency of 0.5 Hz was chosen so to have a negligible drift during the I-V measurement. Furthermore, the laser beam illuminating the AFM tip was modulated with an optical chopper at the frequency of 371 Hz. This frequency was chosen as far enough from both the low frequency acoustic noise and the AC power lines frequency at 60 Hz. A post processing procedure was adopted to build the I-V characteristic, by using the currents read at the same position both in dark and illuminated conditions.

Finally, the acquired data were considered meaningful only upon comparison of a sequence of consecutive readings, thus to assure the reproducibility of the data.

Type 2 measurement: The current output from the analogic filter was given as input to the Stanford dual channel lock-in amplifier while the optical chopper TTL output was used as reference. In this way, only the signal locked in-phase with the reference frequency was amplified whereas the remaining signals were suppressed. Essentially, this method was employed to discern and acquire the signal directly correlated (in-phase) with the illumination.

IM2 surface roughness

In **Figure S2** is shown the measured surface roughness of a Ti film deposited on the quartz substrate, resulting in a range of only 1-2 nm. This measurement was performed in contact mode with a 10-15 nm diameter Si probe. Furthermore, upon growth of native TiO_x or under atomic layer deposited (ALD) TiO_2, the surface roughness maintains similar values (not shown).

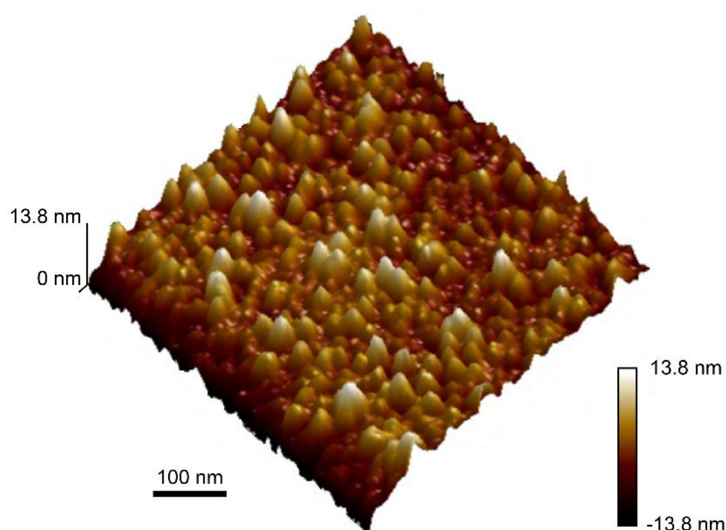

Figure S2. Surface topography of titanium metal with native oxide on the top. The overall area is 500 nm x 500 nm.

Force vs. photocurrent maps

The AFM cantilever probe pressing on the TiO_x/Ti substrate results in a foot print whose area depends on the applied force. While this force can be freely adjusted, the remaining parameters contributing to the foot print area, such as the dimensions of the nanocone apex, the occurring adhesion between the substrate and the probe, the surface roughness, the elastic moduli and the Poisson ratios of the tip and substrate, cannot be changed during the

experiment. These considerations are motivated by observing that the contact area between the nanocone and TiO_x/Ti substrate defines the capacitance in our rectenna junction, thereby it directly affects the rectification performance. To study the role of the contact area on the rectification process, we have acquired photocurrent maps on a TiO_x/Ti substrate with three different forces, where the force amplitude in the AFM software is chosen through a set point parameter. In particular, we used three force set points -0.25, -0.1, 0.2 (increasing force) where the lowest value corresponds to a force limit configuration as sometimes the cantilever is seen to retract away from the substrate. In order to compare the photocurrents recorded for the three selected forces on the same sample, we had first to minimize the X and Y thermal drifts, a goal that was achieved by simply scanning in contact mode the substrate without making any measurements. Afterwards, Type 2 measurements were initiated to measure the photocurrent.

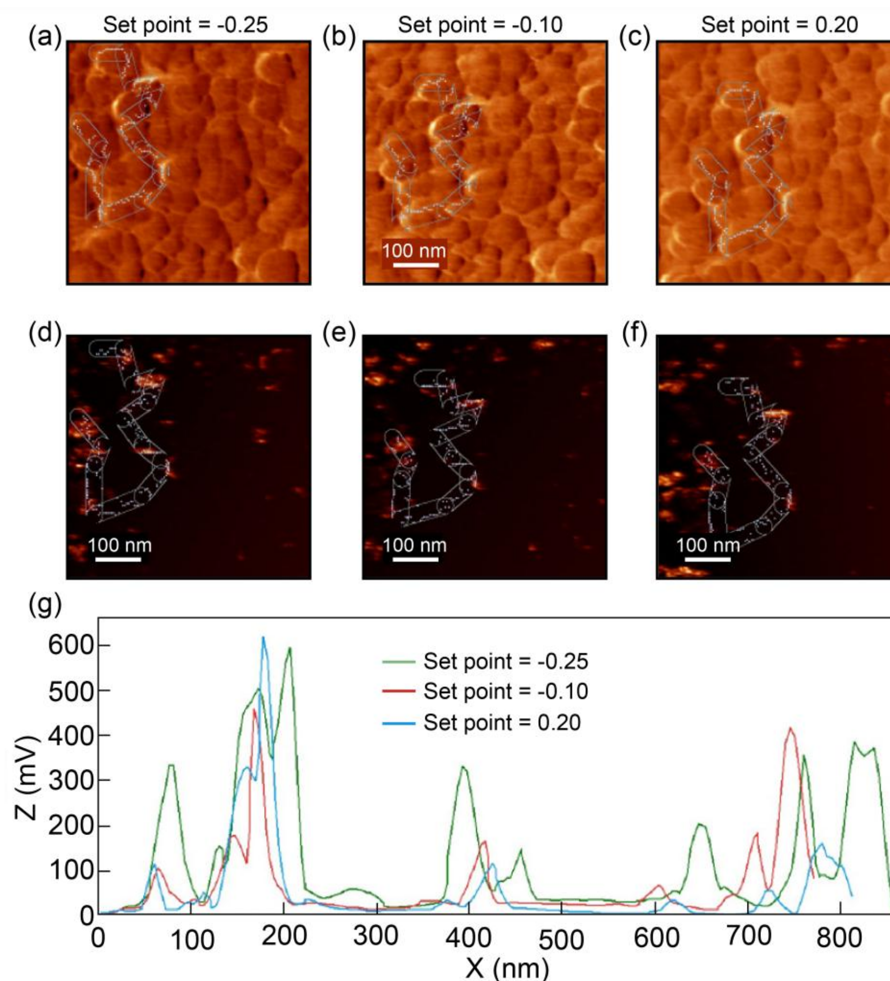

Figure S3. Friction maps (a, b, c) and corresponding photocurrent maps (d, e, f) for three different force setpoints equal to -0.25, -0.10 and 0.20. (g) Photocurrents along the zig-zag line profile swept on the sample shown in (d-f) with force setpoints of -0.25 (green colour line), -0.10 (red colour line) and 0.20 (blue colour line).

For an easy comparison of the three force-related maps, we chose to report friction maps (friction refers to the lateral deflection signal due to the torque experienced by the AFM cantilever while scanning on the substrate) instead of height maps as the former could better describe the substrate morphology. **Figures S3a**-f illustrate friction and the corresponding photocurrent maps for the three aforementioned set points, where a zig-zag scanning profile was chosen. Figure S3g depicts instead the comparison of the photocurrent profiles for the three set points, with the lowest contact force set point -0.25 (green line) showing averagely higher magnitude with respect to -0.1 (red line) and 0.2 (blue line) set points. This result suggests that a small footprint, as determined by a weak applied force, is indeed the best configuration for achieving higher yield of rectified current.

In order to quantify the forces associated to the chosen setpoints, we have performed a separate study of force-distance measurements on different TiO_x/Ti substrates. The forces corresponding to the chosen setpoints are found of the order of few nanonewtons (see **Table S3**), small enough to avoid indentation of the samples. The contact radius C_r values on the substrates under different forces were then deduced from the Derjaguin-Muller-Toporov (DMT) model[1,2], where the nanocone tip-apex is assumed to be a sphere in contact with a planar surface. In particular, we adopted the DMT model owing to the use of a nanocone with a small tip radius, to the presence of a not negligible adhesive contact between tip and substrate, and to the employment of a small load on the substrate. The equivalent Young's modulus (E*) for the joint pc-M1IM2 rectenna (pc-M1 as gold, I as TiO_x, M2 as Ti) is given by:

$$\frac{1}{E^*} = \frac{1 - \nu_{\mathrm{Au}}^2}{E_{\mathrm{Au}}} + \frac{1 - \nu_{\mathrm{TiOx}}^2}{E_{\mathrm{TiOx}}}$$

Here we considered the bulk values for the Poisson ratios v for Au and TiO_x, which are 0.42 and 0.28, respectively. Furthermore, the gold over layer deposited on top of the carbon-platinum composite cone is defined by a thin film of 20-25 nm, hence characterized by a Young's modulus (E_{Au}) different from bulk gold material. In particular, as reported by Salvadori *et al.*[3] who analysed especially thin films of gold on AFM probes, the value for E_{Au} is 69.1 GPa. Similarly, the Young's modulus of Titania (E_{TiO2}) decreases drastically for thin films and it depends significantly on the material density. Since the Young's modulus of very thin films of TiO_2 is not reported in literature, we considered two extreme situations, i.e. the Young's modulus for bulk medium (282 GPa[4]) and for thin films realized through

Atomic Layer Deposition (169.6 GPa[5]). Finally, the contact radius C_r under force F produced with a tip of diameter D is given by:

$$C_r = \left(\frac{3FD}{4E^*}\right)^{\frac{1}{3}}$$

Table S3 summarizes the forces and their corresponding contact radius values for the three different set points -0.25, -0.1, 0.2 when the Young's moduli of TiO_x (ALD titania) and bulk TiO_2 are considered together with a tip radius of 25 nm.

Set point	Force (nN)	Contact radius (nm) Thin film	Contact area (nm^2)	Contact radius (nm) Bulk material	Contact area (nm^2)
-0.25	10.5 ± 0.45	1.27 ± 0.09	5.07 ± 0.71	1.21 ± 0.08	4.64 ± 0.65
-0.10	11.3 ± 0.38	1.30 ± 0.09	5.30 ± 0.71	1.24 ± 0.08	4.87 ± 0.65
0.20	13.1 ± 0.08	1.36 ± 0.08	5.86 ± 0.70	1.30 ± 0.07	5.36 ± 0.61
-0.10 (elastic softening)	11.3 ± 0.38	1.45 ± 0.10	6.63 ± 0.90	1.41 ± 0.09	6.22 ± 0.83

Table S3. Summary of contact radius evaluated for Au nanocones in contact with TiOx/Ti when three different forces were considered. The contact area describes a circular area of radius equal to the corresponding contact radius.

In particular, the -0.1 set point was used throughout the I-V experiments (in fact, the -0.25 set point might have sounded as a better choice, however in some situations we found that the AFM probe was not properly reacting under such a low value set point). Importantly, it was found that, through the DMT model, the -0.1 set point was resulting in a contact radius of 1.27 nm, a value falling in the same number range as from the Simmons fit of the I-V curve. This contact radius value was then adopted in all the numerical simulations (in fact, it was 1.3 nm). For completeness, considering the elastic softening effect of the gold tip due to its grains, we have also considered a smaller value for the Au Young's modulus, in fact as small as 44 GPa[3], thus resulting in an increase of the contact radius up to 1.45±0.10 nm, as reported in the last row of Table 3. Importantly, our simulations (not shown) have highlighted the minimum change in the absorption value occurring when the Cr is changed from 1 nm to 2 nm. In particular, a maximum decrease of 1 % is found for 780 nm, whereas for 1064 nm a maximum increase of 10 % is observed. These results suggest that the aforementioned changes of C_r are not going to appreciably influence the absorption value, hence it is expected

that the efficiency might change simply due to different values of the photocurrent, as seen in Figure S3g.

I-V characteristics for TiO_2 ALD layer

Nanorectennas prepared with ALD grown TiO_2 were also studied for comparison with the native oxide. Oxides of thicknesses 0.5 nm and 1.0 nm were deposited on top of Ti substrate. In particular, a thin conformal layer of TiO_2 was deposited at 200 °C by means of an Oxford Instrument FlexAl Atomic Layer Deposition System following a very slow deposition rate (0.045 nm/cycle). After the deposition of the oxide, a long cooling ramp (4 hours) was adopted to avoid any thermal stress. The I-V characteristics for the 0.5 nm and 1.0 nm samples at λ = 1064 nm are presented in **Figure S4**.

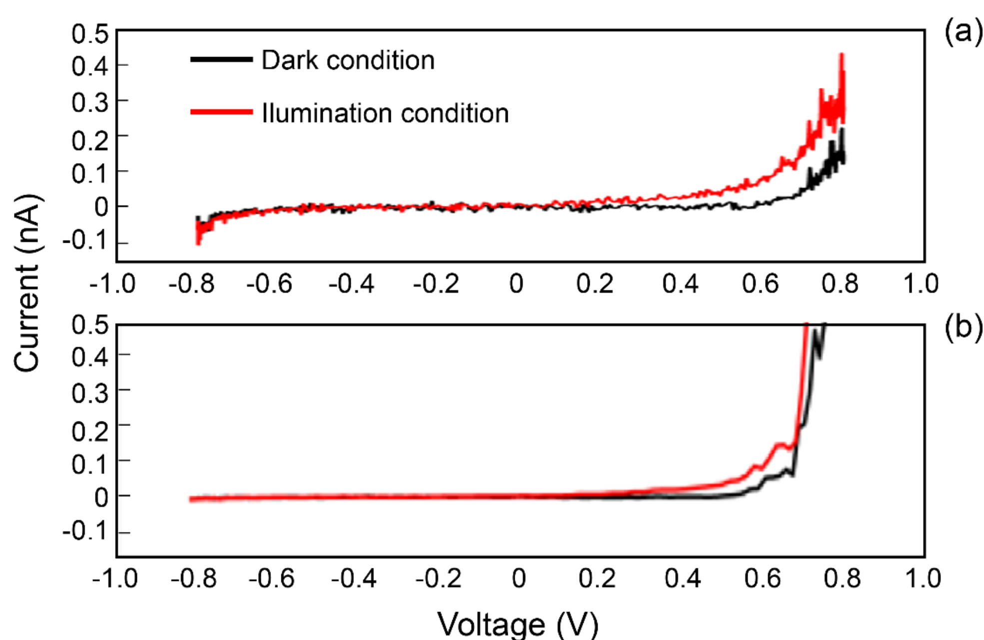

Figure S4. (a) I-V characteristic for 0.5 nm of ALD-TiO_2. (b) I-V characteristics for 1.0 nm of ALD-TiO_2. For both cases λ = 1064 nm.

Both cases confirm the negligible presence of the reverse leakage current, as indeed expected for an ideal diode. Additionally, a strong asymmetry is found in the voltage-current curve. Interestingly, the V_{oc} and I_{sc} values are smaller than the native oxide counterparts, which is possibly due to the improved conductivity of non-stoichiometric oxides (TiO_x) due to oxygen vacancies.[6] This result suggests that the actual conductivity of the insulating layer might play a more important role than its thickness.

I-V characteristics at wavelength 780 nm

In order to investigate the feasibility of our nanorectenna in the visible frequencies, experiments were performed with also 780 nm wavelength. A solid state diode pumped laser was employed together with a single mode fibre for spatial filtering of the higher order modes. The resulting I-V characteristic, when a 7.10 MW/m^2 input intensity was reaching the sample, is shown in **Figure S5a**. Similar to the 1064 nm case, the current measured under illumination conditions is higher than the dark condition counterpart, which suggests light rectification also at 780 nm through our pc-M1IM2 nanorectenna. The small difference between light-on and light-off conditions at V = 0 (see inset in Figure S5a) infers about the weak coupling occurring between the incident radiation and the nanorectenna, an expected situation as the antenna was designed for 1064 nm. In this regard, it is interesting to compare the near field calculated at the tip apex when λ=780 nm and λ=1064 nm are considered, as shown in Figure S5b and S5c. The figures clearly demonstrate a stronger electric field norm (about a factor 3) at λ= 1064 nm, therefore suggesting a better resonance matching of the cone at this wavelength, as already confirmed by the absorption calculations shown in the main text.

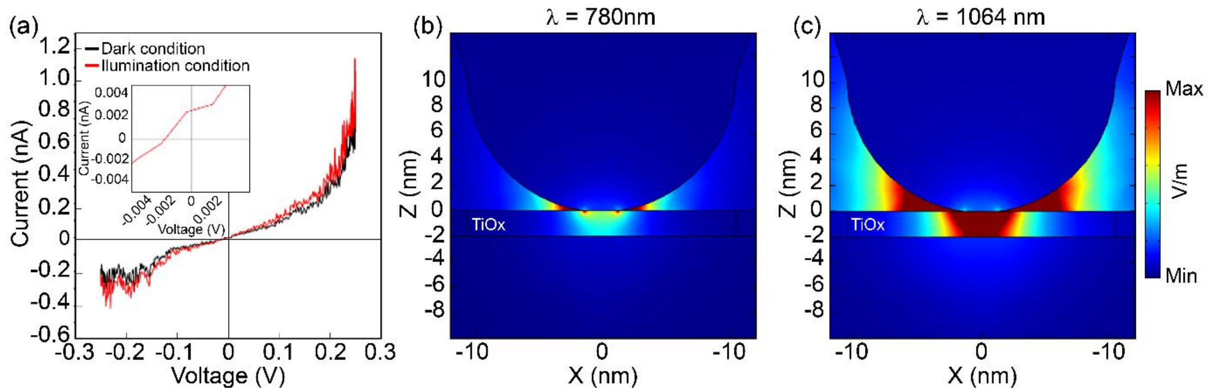

Figure S5. (a) Experimental I-V characteristic for a single nanorectenna at λ = 780 nm. Here, I_{SC_780nm}= 2.58 pA and V_{OC_1064nm} = 2.2 mV obtained with an input intensity equal to 7.10 MW/m^2. (b) Electric field norm calculated at 780 nm starting from an incident field of 1 V/m. (c) Similar to (b) but at λ = 1064 nm.

In terms of efficiency, by considering the experimental input intensity at λ = 780 nm equal to 7.10 MW/m^2 with a t_{Au} = 20 nm, the full cone returned an absorption of 0.21 μW leading to an efficiency of 6.7×10^{-7} %, equal to the value obtained when the geometrical cone cross section was considered (i.e., optical cross section ~ geometrical cross section). Similarly, when only the Au tip was utilized for evaluating the absorbed power, the calculated absorption was equal to 0.0015 μW leading to an efficiency equal to 9.5×10^{-5} %, as reported in Figure 5, main text.

Opto-thermal simulations

In order to rule out the presence of thermal effects in our structure, we performed a FEM based opto-thermal analysis taking into account both the geometry and the material properties as in the experiment. Our calculations reveal that the temperature rising at the nanocone apex under illumination condition never overcomes 2 K with respect to the room temperature. In particular, the highest temperature increase is observed at 1064 nm, whereas at 780 nm a 0.7 K increase is obtained. The temperature distribution on the nanocone is illustrated in **Figure S6**, ranging from about 2 K increase at the nanocone apex down to close-to-zero K variation at the TiO_2 layer. This result suggests the absence of any contribution from thermal expansion, Seebeck effect and thermal assisted tunnelling. Indeed, 2 K temperature rise on the nanocone, even assuming it was associated to the entire nanocone and not just to its apex, would produce a thermal induced expansion of less than 0.01 nm (here Au thermal expansion coefficient of $14 \cdot 10^{-6}$ K^{-1} is assumed). Furthermore, it is well known that the Seebeck effect predicts a voltage variation for each ΔT= 1 K of the order of μV. The measured V_{OC} is instead much higher, of the order of mV (in fact, from a few mV at 780 nm up to 150 mV at 1064 nm). Finally, any kind of thermal assisted tunnelling effect should rely on just 2 K energy, corresponding to 0.17 meV. By considering the MIM barrier height equal to U_0= 3.94 eV and width W=1.5 nm (see main text), and recalling the tunnelling probability $T = e^{(-2bW)}$ with $b = (2m(U_0-E)/\hbar^2)^{1/2}$ and E= electron energy (due to the temperature rise – 2 K - and to the energy coming from absorbed photon - 1064nm=1.17eV -), it can be found that the difference between T with/without the thermal contribution is virtually zero.

Clearly, due to the very small temperature increase, any thermal contribute can be ruled out from the nanorectenna system, as already suggested in the main text.

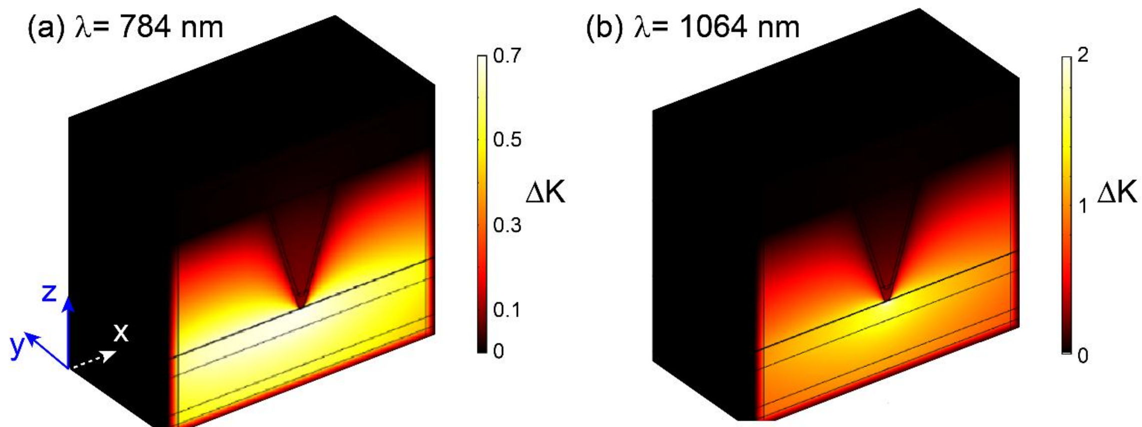

Figure S6. Temperature distribution of the nanocone. (a) λ = 780 nm and input intensity equal to 7.10 MW/m^2. (b) λ = 1064 nm and input intensity equal to 12.95 MW/m^2. For both cases cone height 300 nm, cone base 200 nm, t_{Au} = 20 nm, apex radius 10 nm, Cr = 1.3 nm. The IM2 layer is formed by 2 nm of TiO_x and 50 nm of Ti.

Oxidation kinetics using ellipsometric data

Through native oxidation, TiO_x was grown on top of a Ti (50 nm)/quartz substrate inside an ISO 6 cleanroom, the overall system kept at room temperature. Spectroscopy Ellipsometry measurements in the 400-1500 nm range, using a J. A. Woollam Co., inc. V-vase system, revealed a TiO_x layer thickness < 2nm on top of Ti with less than 1 nm surface roughness, hence confirming our previous AFM analysis. The sample was subjected to several periodic measurements over time starting 10 min after deposition, resulting in a progressive increase of the oxide layer thickness as depicted by the fit in **Figure S7**. As for the TiO_x optical functions the refractive index is given in the WVASE software database best-fitted to a Cauchy model $n= A + B/\lambda^2 + C/\lambda^4$ (A=2.1679, B= 0.01054, C=0.00265), and extinction coefficient k negligible in the considered spectral range. The fitting follows literature growth model for Ti oxidation[7,8] and, as referred in literature,[9,10] the nature of the native oxide consists of multiple layers of non-stoichiometric oxides with the external one showing a stoichiometric oxide nature (TiO_2). Non-stoichiometric oxides are especially known to display good conductivity due to oxygen vacancies, an important aspect for rectenna applications.

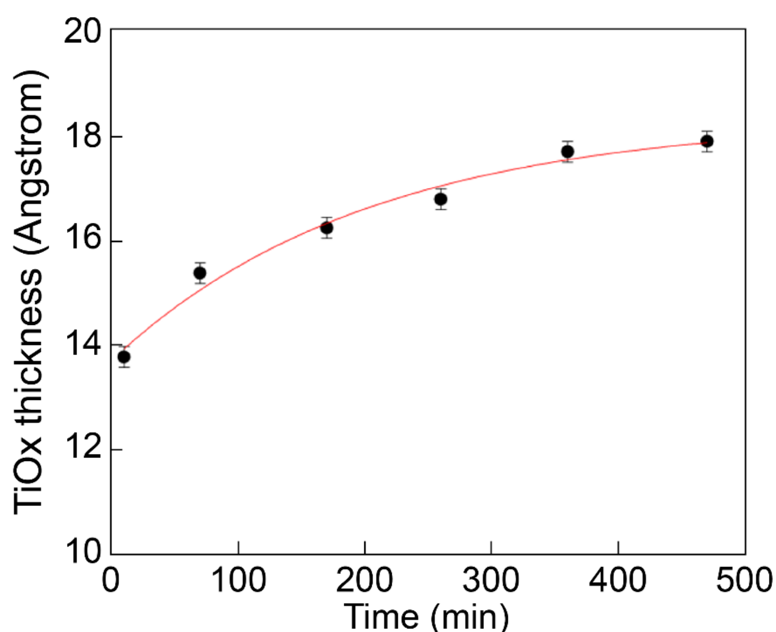

Figure S7. TiO_x thickness growth over time during the oxidation process of Ti film.

XPS data of native Ti oxide

X-ray photoelectron spectroscopy (XPS) measurements were performed 2 hours after Ti deposition on quartz confirming the formation of titanium oxide on top of the Ti surface, as shown in **Figure S8**. From the figure it can be noticed that the main peak Ti $2p_{2/3}$ at ~458.6 eV can be attributed to Ti^{4+} (Ti(IV) in the legend) which is mainly related to stoichiometric TiO_2. The secondary peak at ~464.4 eV is instead Ti $2p_{1/2}$. The successive peaks at lower energies can be associated to sub-stoichiometric species Ti_2O_3 (attributed to Ti^{3+}=Ti(III)), TiO (attributed to Ti^{2+}=Ti(II)) and metallic Ti. These findings suggest about the formation of an oxide layer composed by 5.5 % of TiO, 21.5 % of Ti_2O_3 and 64% of TiO_2. The results are coherent with previously reported data of native oxidation of Ti surfaces.[8]

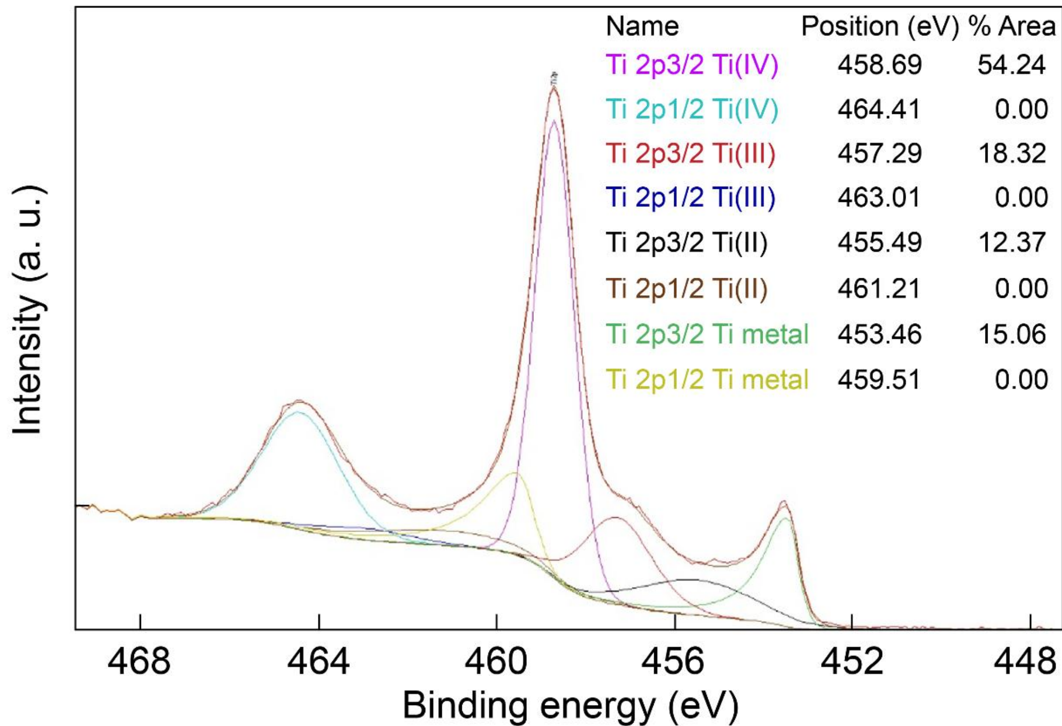

Figure S8. XPS spectra of native TiO_x layers.

Theoretical model and fit

The Simmons' model is one of the most widely employed general analytical models being employed to describe the J-V characteristic (J current density, V applied potential) of a tunnelling junction in dark conditions[11-13]. The Simmons' model is based on the parameters describing the junction, namely the barrier height and thickness. Based on the quantum mechanical Wentzel-Kramers-Brillouin approximation, it can provide an analytical expression for one dimensional transport across a tunnelling barrier of arbitrary shape and average effective height defined as $\overline{\phi}$: [14]

$$J(V) = J_0\bar{\phi}e^{-A\bar{\phi}^{1/2}} - J_0(\bar{\phi} - eV)e^{-A(\bar{\phi}+eV)^{1/2}} \quad \text{(S1)}$$

Here $J_0= e/(2\pi h(\beta\Delta s)^2)$ and $A= 4\pi\beta\Delta s/h\sqrt{(2m^*)}$, with Δs the effective barrier thickness and m* the electron effective mass. The parameter β defines how well the barrier height profile can be replaced by its average, with Simmons justifying $\beta \approx 1$ for trapezoidal barrier structures and asymmetric material junctions. In Equation S1, the first and the second addends describe the forward and reverse current, respectively.

By knowing the barrier profile and the materials properties of the system, one can therefore determine the tunnelling current in dark conditions. In an attempt to keep complexity at a minimum, we considered a simplified trapezoidal barrier without image force. This choice is supported by the fact that the relevance of the image potential term is limited for thin barriers,[12] as in our case (< 2 nm TiOx barrier). Furthermore, for point contact-insulator-metal geometries, the one dimensional energy diagram acquires a concave/convex shape as shown in Nguyen *et al.*,[15] with a bending less pronounced for smaller tip radii therefore leading to a more rectangular-like barrier.[16]

Equation S1 can be linked to the measured tunnelling current I by the expression $I = J\cdot S$, with S the tunnelling area.[14] In the intermediate voltage range ($V < \phi/e$), it can be written as:

$$I = S\frac{e}{2\pi h d^2}\left[\left(\phi - \frac{eV}{2}\right)e^{-\frac{4\pi d\sqrt{2m^*}}{h}\sqrt{\phi-\frac{eV}{2}}} - \left(\phi + \frac{eV}{2}\right)e^{-\frac{4\pi d\sqrt{2m^*}}{h}\sqrt{\phi+\frac{eV}{2}}}\right] \quad \text{(S2)}$$

where d the barrier thickness. By the least square method fit we can finally retrieve the barrier height, the barrier thickness and the tunnelling area. As noted, given its approximated nature, the model parameters are an estimation of real parameters (not-exact). Despite this, and similar to Kern *et al.*,[13] Simmons' model is shown to provide a reasonably good description of the tunnel junction. The model presented here is however limited to the intermediate voltage range where the I-V curve can be described by a central symmetric curve. In our case this assumption is verified as the barrier height retrieved by the fitting of Equation S2 returns indeed a ϕ value of 3.94 eV, higher than the applied voltage falling in the range between -0.2 V and 0.2 V, as shown in Figure 3a and Figure 4b.

[1] B. Cappella, G. Dietler, *Surf. Sci. Rep.* **1999**, *34*, 1–104.

[2] U. Celano, T. Hantsche, G. Giammaria, R. C. Chintala, T. Conard, H. Bender, W. Vandervorst, *J. Appl. Phys.* **2015**, *117*, 214305.

[3] M. C. Salvadori, I. G. Brown, A. R. Vaz, L. L. Melo, M. Cattani, *Phys. Rev. B* **2003**, *67*, 153404.

[4] J. F. Shackelford, Y. H. Han, S. Kim, S H. Kwon, *CRC Materials Science and Engineering Handbook*, CRC Press, **2015**.

[5] J. Lyytinen, X. Liu, O. M. E. Ylivaara, S. Sintonen, A. Iyer, S. Ali, J. Julin, H. Lipsanen, T. Sajavaara, R. L. Puurunen, J. Koskinen, *Wear* **2015**, *342–343*, 270-278.

[6] I. Z. Mitrovic, S. Almalki, S. B. Tekin, N. Sedghi, P. R. Chalker, S. Hall, *Materials* **2021**, 14, 5218.

[7] M. C. Burrell, N. R. Armstrong, *Langmuir* **1986**, *2*, 30-36.

[8] G. Droulers, A. Beaumont, J. Beauvais, D. Drouin, *J. Vac. Sci. Technol.* B **2011**, *29*, 021010.

[9] J. Pouilleau, D. Devilliers, F. Garrido, S. Durand-Vidal, E. Mahé, *Materials Science and Engineering: B* **1997**, *47*, 235-243.

[10] M. M. Pedemonte, A. L. Capparelli, *Energy Pow. Eng.* **2015**, *7*, 403-411.

[11] F. Wang, N. A. Melosh, *Nature Comm.* **2013**, *4*, 1711.

[12] C. Lee, I. I. Nedrygailov, Y. K. Lee, C. Ahn, H. Lee, S. Jeon, J. Y. Park, *Nanotechnology* **2015**, *26*, 445201.

[13] J. Kern, R. Kullock, J. C. Prangsma, M. Emmerling, M. Kamp, B. Hecht, *Nature Phot.* **2015**, *9*, 582-586.

[14] J. G. Simmons, *Journal of applied physics* **1963**, *34*, 1793-1803.

[15] H. Nguyen, P. Cutler, T. E. Feuchtwang, Z.-H. Huang, Y. Kuk, P. Silverman, A. Lucas, T. E. Sullivan, *IEEE Trans. on Electr. Devices* **1989**, *36*, 2671-2678.

[16] P G. Fursey, D. Glazanov, *J. Vac. Sci. & Tech. B* **1995**, *13*, 1044–1049.